High oscillator strength interlayer excitons in two-dimensional heterostructures for mid-infrared photodetection

Lukman, Steven; Ding, Lu; Xu, Lei; Tao, Ye; Riis-Jensen, Anders C.; Zhang, Gang; Wu, Qing Yang Steve; Yang, Ming; Luo, Sheng; Hsu, Chuanghan

Total number of authors:
18

Published in:
Nature Nanotechnology

Link to article, DOI:
10.1038/s41565-020-0717-2

Publication date:
2020

Document Version
Early version, also known as pre-print

High Oscillator Strength Interlayer Excitons in 2D Heterostructures for Mid-IR Photodetection

Steven Lukman[1], Lu Ding[1], Lei Xu[2], Ye Tao[3], Anders C. Riis-Jensen[4], Gang Zhang[5], Qingyang Steve Wu[1], Ming Yang[1,2], Sheng Luo[6], Chuanghan Hsu[6], Liangzi Yao[7], Gengchiau Liang[6], Hsin Lin[7], Yong-Wei Zhang[5], Kristian S. Thygesen[4], Qi Jie Wang[3], Yuanping Feng[2], Jinghua Teng[1]

[1]Institute of Materials Research and Engineering, Agency for Science, Technology and Research (A*STAR), 2 Fusionopolis Way, Innovis, Singapore 138634.

[2]Department of Physics, National University of Singapore, 2 Science Drive 3, Singapore 117551.

[3]School of Electrical and Electronic Engineering, Nanyang Technological University, 50 Nanyang Avenue, Singapore 639798.

[4]CAMD and Center for Nanostructured Graphene (CNG), Department of Physics, Technical University of Denmark, DK-2800 Kongens Lyngby, Denmark.

[5]Institute of High Performance Computing, Agency for Science, Technology and Research (A*STAR), 1 Fusionopolis Way, Connexis, Singapore 138632.

[6]Department of Electrical and Computer Engineering, Faculty of Engineering, National University of Singapore, Singapore 117583

[7] Institute of Physics, Academia Sinica, Taipei 11529, Taiwan

Correspondence and request for materials should be addressed to J.H.T (email: jh-teng@imre.a-star.edu.sg).

Keywords: 2D materials, 2D heterostructure, interlayer exciton, interface exciton, oscillator strength, orbital overlap, mid-IR photodetector, WS_2, HfS_2

Abstract:

The development of infrared (IR) photodetector is mainly limited by the choice of available materials and the intricate crystal growth process. Moreoever, thermally activated carriers in traditional III-V and II-VI semiconductors enforces low operating temperatures in the IR photodetectors. Here, we demonstrate IR photodetection enabled by interlayer excitons (ILEs) generated between tungsten and hafnium disulfide, WS_2/HfS_2. The photodetector operates at room temperature and shows even higher performance at higher temperatures owing to large exciton binding energy and phonon assisted optical transition. The unique band alignment in WS_2/HfS_2 heterostructure allows interlayer bandgap tuning from mid- to long-wave infrared. We postulate that the sizeable charge delocalisation and ILE accumulation at the interface result in greatly enhanced oscillator strength of ILEs and high responsivity of the photodetector. The sensitivity of ILEs to the thickness of two-dimensional materials and the external field provides an excellent platform for realising robust tunable room temperature IR photodetectors.

Mid- and long-wavelength infrared (MW-LWIR) photodetectors have been found useful for many important applications, such as in medical, security, surveillance and material evaluation. A photodetector consists of light-sensitive material that can absorb electromagnetic radiation, which subsequently converts the photons into measurable current. In the MW-LWIR regime (3-15 μm), corresponding to photon energy around 83-413 meV, there are only a handful of narrow bandgap semiconductors that are suitable for this purpose. The widely available IR photodetectors are made of III-V and II-VI compound semiconductors, such as $Hg_{1-x}Cd_xTe$, $In_{1-x}Ga_xAs$, and InSb[1]. However, delicate and expensive processes are required to grow these compounds and the lattice matching between materials and substrate further limits their availability.

The performance of IR photodetectors is largely determined by charge-generation efficiency from absorbing impinging photons on the active region, the lifetime and mobility of the charge carriers, as well as the dark current from thermally activated carriers. Small binding energy (E_b < 25 meV)[2,3] of electron-hole pairs (excitons) in conventional narrow bandgap IR photodetectors means thermal energy at room temperature (25 meV) is sufficient to overcome it, thus excitons spontaneously dissociate into free-carriers once formed. Similarly, the thermal-carrier generation and lattice phonon is evident at room temperature. Therefore, the IR-generated carriers can easily decay to ground state in the absence of cooling[1,4,5]. These processes shorten the carrier lifetime and prevent charge extraction that eventually lowers the efficiency of photodetectors, especially at higher temperatures. The necessity to operate at substantially reduced temperatures to suppress these processes complicates the detector architecture and limits their sensitivity at room temperature.

For the past few years, 2D materials and their heterostructures have emerged as a promising platform for electronic and optoelectronic applications, with a particular interest in transition metal dichalcogenides (TMDs) semiconductors[6-10]. The out-of-plane van der Waals (vdW) bond in 2D materials is advantageous as it allows the 2D materials to be fabricated on any substrate without a lattice-matching constraint. Subsequently, the absence of dangling bonds on the surface would eliminate dark current from surface-recombination, which is ideal for photodetectors. 2D semiconductors have strongly bound excitons due to strong quantum confinement and reduced dielectric screening[11,12]. The recombination of electron and hole, i.e. the decay of exciton, is limited by resonance stabilisation due to the overlap of electron and hole wavefunctions, resulting in an extended lifetime for the exciton[5,13]. The indirect bandgap character of many 2D semiconductors benefits from phonon at higher temperature, which aids in momentum conservation upon photo-

absorption. Therefore, the thermal effect could potentially have positive effect for IR photodetectors based on 2D semiconductors. Furthermore, 2D semiconductors have been shown to integrate easily with metals[14] or graphene[15], which makes them suitable for optoelectronic applications as facile carrier extraction or injection sites.

Graphene has attracted numerous interests in MW-LWIR detection due to its broadband absorption and high carrier mobility. However, the low-absorption coefficient, high dark current, and short-carrier lifetime hamper the performance[16]. An intrinsically narrow-bandgap black phosphorus (b-P)[17,18], shows thickness and electrostatic-gating bandgap dependent adjustable from 0.2 to 2.0 eV (0.62-6.2 μm). The bandgap can be further extended down to 0.15 eV (8.3 μm) by alloying with arsenic (b-AsP)[19,20]. However, this material is not thermodynamically stable. Alternatively, a handful of narrow-gap TMDs semiconductors with $E_g < 1$ eV have also emerged recently as promising candidates for IR detectors, such as (Zr, Ni, Pd, Pt, Bi)Se_2/Te_2[21]. Nonetheless, the difficulty in fabrication and controlling the band-gap impose greater challenges on their practical applications[22-24].

When two dissimilar TMDs semiconductors are stacked together to form a type-II heterostructure, a space-indirect interlayer exciton (ILE) will form through charge hopping between materials. These ILEs have large E_b[25,26,27], which is comparable to the intralayer excitons generated within parent materials[11,12]. The photo-active range of ILEs is determined by the band-energy alignment of the constituent material, which offers the potential to utilise ILE for tunable IR photodetector. Nevertheless, the space-indirect character of ILE renders it with a weak optical absorption[25,26,28]. Here, we explore the unique properties of ILEs in 2D TMD HETEROSTRUCTURE formed between WS_2 and HfS_2 and demonstrate a highly-responsive room temperature operated MW-LWIR photodetector with tunable detection range. Based on the study of the thickness dependence, response to electric field and excitation density, and *ab initio* calculations, we postulate that the observed ILE have the same order of oscillator strength as intralayer excitons. Enhanced spatial orbital overlap and phonon-assisted momentum conservation favour the optical transition of ILE. The findings here provide insights for tailoring ILEs for optoelectronic applications that offer a promising way to make a compact and efficient room-temperature photodetector that can be extended down to far-IR.

Formation and Characteristic of Interlayer Exciton. The conduction band minimum (CBM) and valence band maximum (VBM), relative to vacuum[24], of monolayer WS_2 and HfS_2 are illustrated in Fig. 1a. HfS_2 (d^0 semiconductor) is chosen for this study because it has a deep CBM and high electron mobility, which is favourable for ILEs electrons to reside when paired with d^2 semiconductors (i.e. WS_2)[29]. HfS_2 of different thicknesses are laid on top of monolayer WS_2 to maintain direct band-gap for optical excitation. For subsequent discussion, the thinner and thicker HfS_2 refer to ~3 and 30 layers (bulk), respectively, unless otherwise specified.

The optical responses of individual TMDs and the heterostructures are plotted in Fig. 1b. The reported absorbance has been calculated from the differential reflectance contrast of the flakes and normalised to the thickness (detail in Supplementary Info.). The A exciton peak, which is associated with the band-edge transitions in monolayer WS_2, centers around 2.04 eV. This value is close to the previously reported value[30]. On the other hand, HfS_2 is an indirect-bandgap material, the band gap is inferred from extrapolation to the abscissa. We notice the main excitonic peaks at heterostructures are slightly broadened and red-shifted (1.94 eV) compared to the parent materials. The observed broadening, $\Delta\Gamma$, is associated with shortening lifetime of the photo-generated excitons as $\tau = \hbar/\Delta\Gamma$[31] (where $\hbar$ = is the Planck constant) due to charge hopping at the interface.

Interestingly, the heterostructure has an additional strong absorption peak in the lower energy region as shown in Fig. 1b, which is not present in the constituent materials. The heterostructure peaks are centred at 0.24 eV for WS_2-3L HfS_2 and 0.21 eV for WS_2-bulk HfS_2. The absorption becomes stronger and red-shifts with increasing layers of HfS_2 (Extended Data Fig. E1). These low-energy absorptions show no obvious sample angular-dependence (Extended Data Fig. E2). Furthermore, the peak energy is responsive to an external electric field (Fig. 1c). The gate dependence suggests these peaks are associated with ILEs, with dipole moment pointing from HfS_2 to WS_2 substantiating the charge transfer at the interface. Strong intralayer exciton quenching of WS_2 (Supplementary Info Fig. S4) also suggests electron transfer to HfS_2[32,33]. We can rule out the possibility of energy transfer as photoluminescence (PL) of HfS_2 decreases compared to bare HfS_2.

Exciton Accumulation and Band Structure at Interface. The ILEs PL (λ_{exc} = 532 nm) is prominent even at room temperature, demonstrating robust radiative recombination. The PL spectral shape changes with thickness of HfS_2, with thinner HfS_2 consisting of broader emission peak that is made of two Gaussian peaks (Fig. 1d). The energy difference between the two peaks

(Δ_{ILE}) decreases with increasing number of HfS_2 layers and finally merges into one broad peak in bulk HfS_2 (Fig. 1d and Extended Fig. E3). Increasing excitation density results in blue-shifts of overall PL peak (Fig. 1d). The more significant blueshift in WS_2-bulk HfS_2 indicates a stronger excitonic dipole-dipole repulsion[34].

We also found the PL intensity in WS_2-bulk HfS_2 saturates at lower fluence than the thinner counterpart ($8x10^4$ for bulk vs. $5x10^5$ W/μm^2 for 3L, Extended Fig. E4), which confirms more prominent exciton-exciton annihilation in thicker samples. The higher density of ILEs in the WS_2-bulk HfS_2 interface is responsible for the stronger excitonic repulsion and annihilation observed. We fitted the integrated PL intensity with exponential function $I \sim CP^{\alpha}$, with C= constant and P= excitation power, and we obtained $\alpha \sim 0.8$-0.9 (Extended Fig. E4). Although the dependence is sublinear, α is higher than in typical *p-n* junctions (~0.5)[14,34-36] where ILEs favorably separates into charge carriers. The fact that we encounter an unusually higher sublinear power dependence suggests ILEs likely remain as excitons.

Accumulation of ILEs at the interface is also supported by a simple estimation of ILE density via plate capacitor formula[37]. The maximum ILE density based on the blueshift yields a lower boundary value of $n_{ILE} = 4.7x\ 10^{11}$ cm^{-2} and 1.3×10^{12} cm^{-2} for WS_2 with 3L and bulk HfS_2, respectively (detail in Supplementary Info.). These values are comparable to intralayer WS_2 exciton density generated from the same excitation density, which is in the order of 10^{11} -10^{12} cm^{-2}. We postulate the observed high exciton density at the interface is due to band bending, which favors electrons and holes accumulation in HfS_2 and WS_2, respectively.

To verify the interfacial band-bending, we studied the photoresponse of the heterostructure under the illumination of 532 nm laser. The schematic diagram of the device used in this study is given in Fig. 2a. The *I-V* curves under different excitation power are shown in Fig. 2b. Since the metal-TMD junction forms an ohmic contact near-zero voltage (Supplementary Info Fig. S8), the sign of the photovoltage and photocurrent correlates with the band structure at the interface. The photocurrent shifts the *I-V* curve into the second quadrant, which suggests that carriers accumulate near the junction, instead of being depleted as in typical *p-n* diode.

Band bending at heterostructure of 2D materials is possible and has been verified experimentally[38-40]. The band bending at the heterostructure junction is dependent on the relative Fermi energy level and carrier concentration at the junctions. If we assume similar Fermi energy level for 3L- and

bulk HfS_2, the magnitude of band bending in both cases is expected to be similar, yet with narrower depletion width in 3L-HfS_2 as space is more constraint than in bulk-HfS_2 (Fig. 2c). We performed a theoretical calculation to estimate the band bending diagram through a self-consistent calculation for charge density and potential in real space, the results are plotted in Fig. 2d (for 3L-, 5L-, and 7L-HfS_2/WS_2). The change in band bending when external bias is applied is shown in Extended Data Fig. E5. The reduction of bandgap in bulk HfS_2 is mainly reflected as the upward shift of VBM of HfS_2 as the CBM hardly changes with thickness (Supplementary Info. Fig.S17). In this model, we assume the band bending in monolayer WS_2 is small or non-existent as it is physically not practical. The model clearly shows increasing depletion width with the number of HfS_2 layers.

The aforementioned junction at heterostructure interface act as a trap for ILEs, as illustrated in Fig. 2c, resulting in their accumulation at the interface. These trapped ILEs work as antennas borrowing their oscillator strength, *f,* from the surrounding[41,42]. From a classical viewpoint, when an electron is bound to the nuclear framework and has oscillating dipole, the oscillator strength *f* is directly proportional to the integral over the absorption band. The ILE absorption on this study has the same magnitude as those of intralayer A-exciton (Fig. 1b), thus direct ILE generation via photo-excitation is highly favourable. Accumulation of ILEs also could have enhanced electron-hole overlap at the interface, which overcomes the spatially indirect nature of the transition and contribute to the large *f* as proposed by Lau et al.[43]. To our knowledge, this is the first experimentally observed large interband oscillator strength of ILE in 2D materials[27,44-45], which is generally two orders of magnitude smaller than intralayer exciton *f* due to the spatially separated wave-function. To better understand the nature of optical transition in ILE, we conducted *ab-initio* calculation of the band structure at the heterostructure interface.

Calculated Band Structure at Heterointerface. In type-II heterostructures formed between WS_2 and HfS_2, the VBM of WS_2 shifts from K point to Γ point. The states in K point are mainly built by *d* orbitals of W atom and are hardly affected by HfS_2 due to a large separation between layers. On the other hand, the S-p_z state, which contributes to the occupied states in Γ point, can directly interact with neighboring layers and shifts the VBM to Γ point. However, the maximum energy difference at K and Γ point in WS_2 is very small (Fig. 3a), thus when the spin-orbit coupling is introduced, it raises the energy at K point and moves VBM back to K point (detail in Supplementary Info.) In contrast, the CBM of HfS_2 is unaffected by the hybridisation and remains at M point.

From *ab initio* calculation, we found the hole states at Γ point extend over both WS_2 and HfS_2 layers (Fig. 3b). Hence, the interlayer coupling strength is significant at Γ point due to interlayer hybridisation, and dependent on the thickness of HfS_2. It is worth noting that HfS_2 orbital contribution to VBM increases with the number of layers (color contrast in Fig. 3a), which means the optical transition from Γ to M point becomes less interlayer (more intralayer) in character and the matrix elements for this transition are more favourable. In contrast, the wavefunction overlap at K point is negligible. Therefore, we conclude the observed ILE absorption originates from Γ-M instead of K-M transition despite VBM could be located at K point after hybridization (Fig. 3c). It is worth mentioning that the observed ILEs share certain similarities with interface excitons in lateral heterostructure, partly due to the charge delocalisation and wavefunction overlap.

The large energy difference of CBM and VBM in WS_2 and HfS_2 in our hetero-system results in non-degenerate and non-interacting ILE and intralayer exciton, which explains the small or negligible angular-dependence on the ILE oscillator strength and energy. This outcome is in agreement with previous works by Falko *et al.*[46,47]. In their study, they observed a prominent angular-dependence (Φ) of the ILEs close to 0° and 60° rotation angle due to the strong hybridisation of ILE with intralayer exciton via interlayer conduction-band tunneling.

We further investigated the decrease in the optical band gap of ILE with increasing thickness of HfS_2 by calculating the quasiparticle band gap at the GW level and the ILE binding energy from first-principle calculations for the heterostructure (see Computational Details in Supplementary. Info). The optical band gap can be determined as $E_{gap}^{opt} = E_{gap}^{qp} - E_{b,IE}$, where E_{gap}^{qp} is the quasiparticle bandgap and $E_{b,IE}$ is the ILE binding energy (Fig. 3d). As the consequence of higher dielectric screening with increasing HfS_2 layers, we find that both E_{gap}^{qp} and $E_{b,IE}$ decrease, which results in overall small red-shift of E_{gap}^{opt} (Fig. 3e). Hence, the change in E_{gap}^{opt} is a result of a complex interplay of both factors, which can be manipulated to tune the ILE energy.

Highly Sensitive and Responsive Infrared Photodetector. The enhanced optical properties of ILE at WS_2-HfS_2 heterostructures renders its suitability for IR photodetection. The device structure is shown in Fig. 2a. The device was operated in photo-conductive mode, with the voltage applied between drain and source (V_{ds}) to dissociate ILE and extract free carriers. The photocurrent is defined as $I_{ph} = |I_{ds,illum}| - |I_{ds,dark}|$, where $I_{ds,illum}$ and $I_{ds,dark}$ are current under illumination and dark current, respectively. Figure 4a shows the I-V curve of WS_2-3L HfS_2 when photo-excited

with IR laser (λ_{exc} = 4.7 μm). When a negative voltage is applied to drain relative to the source, I_{ph} increases since charge extraction is favourable under this condition, we called it positive feedback (Fig. 4b, left). Whereas positive V_{ds} confines ILE at the interface, resulting in more recombination (relative to zero V_{ds}) and lower extractable carriers (negative feedback, Fig.4b right). Thicker HfS_2 has larger $I_{ds,dark}$, stemming mainly from stronger confinement and recombination of electrons and holes at the interface. We also find the change in interlayer bandgap energy does not noticeably affect the dark current (Extended Fig. E6). From the current generated, we calculate the responsivity which is defined as ($R = I_{ph}/P_{device}$), where P_{device} is the effective laser power on the sample area, and $P_{device} = P_{in}A_{device}/A_{laser}$, P_{in} is the incident laser power, A_{device} is the effective sample area, and A_{laser} is the laser spot area. Peak responsivity of $8.2x10^2$ AW^{-1} and $9.5x10^2$ AW^{-1} is observed on WS_2-3L HfS_2 upon laser illumination of λ= 4.7 μm and 4.3 μm, respectively at V_g = +40 V (Fig. 4c). With increasing exciton concentration (as P_{device} increases), the I_{ph} and R decrease primarily due to higher exciton scattering and recombination. We notice the thickness of HfS_2 and bias V_g determine the value of R, which is expected as both variables determine the ILE absorption edge.

We analysed the fundamental operating speed of the WS_2-HfS_2 heterostructures photodetector by calculating the average lifetime of the photocarriers in the channel. Using the transit time ($\tau_{transit}$) calculated from the charge carrier mobility (detail in Supplementary Info.), we can estimate the carrier lifetime ($\tau_{lifetime}$) from the photoconductive gain G by using $\tau_{lifetime} = G \times \tau_{transit}$[48]. Figure 4d shows the calculated carrier lifetime of the ILEs under different V_g and excitation power along with the respective fitted values by using the Hornbeck-Haynes model (detail in Supplementary Info.). The calculated response time is ~ 1 ns at V_g= 0 V with V_{ds} = -1.5 V and P_{device} ~ 400 nW. We can also extrapolate the carrier lifetime of the photodetector to an excitation power that is not achievable in our setup. Based on the model, the fundamental response time of ~ 1 ps is possible at P_{device} = 1 mW at V_{ds} = -1.5 V. The fast intrinsic response time is anticipated as HfS_2 and WS_2 have high mobility for electrons and holes transport, respectively[49,50]. Nonetheless, the operating speed of our device is in the millisecond range (Extended Data Fig. E7, E8). It is not the fastest IR photodetectors reported, but we believe there is room for improvement.

Discussion and Future Directions. Figure 5a compares the responsivity of the heterostructures in our study to other 2D-based photodetectors (hybrid 2D-systems are excluded), regardless of their bias voltage and excitation power. The high responsivity of the Mo/W 2D photodetector in visible and near IR range results from the direct-band gap nature of the band-edge excitation. The enhanced absorption of ILE in this study has boosted the responsivity by two orders of magnitudes in the MW/LWIR range, making it comparable to those of Mo/W based photodiode in visible and near IR range (Fig. 5a). Furthermore, the intrinsic dipole of ILE, which is responsive to the externally applied field, can be exploited to dynamically tune the detection range and sensitivity (Fig. 5b).

The calculated detectivity D* of our WS_2-HfS_2 heterostructure photodiode is higher than other commercially available IR photodetectors, especially for room and elevated temperature operation (Fig. 5c). The spectral broadening and increase in phonon-assisted-transition at high temperatures enhance the detection range and detectivity, respectively. We also demonstrated that absorption is tunable and extendable up to 20 μm (0.06 eV) by electrostatic doping, as shown in Extended Data Fig.E9. Theoretically, the absorption bandwidth can be further extended to far-IR (FIR) range, either by applying higher V_g or choosing a suitable combination of materials with the right band alignment. The versatility of ILE in 2D heterostructures is not limited to two materials (AB stacking). Further stacking with similar or dissimilar material on top of the second material would create either ABA or ABC structures (Extended Data Fig. E10). ABA stacking potentially produces a 'quantum well' structure that increases the efficiency further from AB stacking. Whereas ABC stacking allows simultaneous formation of two different ILEs, which could be tailored for either dual photo-detection or -emission system.

Conclusions. In summary, a tunable, highly-responsive and room-temperature MW-LWIR photodetector based on WS_2-HfS_2 heterostructure has been demonstrated. The absorption band can be tuned and extended to 20μm under a modest electric field, far beyond the cutoff wavelength of b-P/b-AsP. Strongly enhanced ILE absorption due to the unique band alignment and orbital hybridisation has contributed to the strong photoresponse. Our study provides a glimpse of the physics of ILEs in the unique heterostructures and offers a promising technology for IR photodetection, and potentially photo-emitter.

References

1 Rogalski, A., Adamiec, K. & Rutkowski, J. *Narrow-gap Semiconductor Photodiodes*. Vol. 77 (SPIE Press, 2000).

2 Iotti, R. C. & Andreani, L. C. A model for exciton binding energies in III-V and II-VI quantum wells. *Semicond. Sci. Technol.* **10**, 1561-1567 (1995).

3 Zrenner, A. *et al.* Indirect excitons in coupled quantum well structures. *Surf. Sci.* **263**, 496-50 (1992).

4 Hu, W. *et al.* Analysis of temperature dependence of dark current mechanisms for long-wavelength HgCdTe photovoltaic infrared detectors. *J. Appl. Phys.* **105**, 104502 (2009).

5 Piotrowski, J. Uncooled operation of IR photodetectors. *Opto-Electron. Rev* **12**, 111-122 (2004).

6 Mak, K. F. & Shan, J. Photonics and optoelectronics of 2D semiconductor transition metal dichalcogenides. *Nat. Photonics* **10**, 216 (2016).

7 Wang, Q. H., Kalantar-Zadeh, K., Kis, A., Coleman, J. N. & Strano, M. S. Electronics and optoelectronics of two-dimensional transition metal dichalcogenides. *Nat. Nanotechnol.* **7**, 699 (2012).

8 Manzeli, S., Ovchinnikov, D., Pasquier, D., Yazyev, O. V. & Kis, A. 2D transition metal dichalcogenides. *Nat. Rev. Mat.* **2**, 17033 (2017).

9 Novoselov, K., Mishchenko, A., Carvalho, A. & Neto, A. C. 2D materials and van der Waals heterostructures. *Science* **353**, aac9439 (2016).

10 Koppens, F. *et al.* Photodetectors based on graphene, other two-dimensional materials and hybrid systems. *Nat. Nanotechnol* **9**, 780 (2014).

11 Cheiwchanchamnangij, T. & Lambrecht, W. R. Quasiparticle band structure calculation of monolayer, bilayer, and bulk MoS_2. *Phys. Rev. B* **85**, 205302 (2012).

12 He, K. *et al.* Tightly bound excitons in monolayer WSe2. *Phys. Rev. Lett.* **113**, 026803 (2014).

13 Kaviraj, B. & Sahoo, D. Physics of excitons and their transport in two dimensional transition metal dichalcogenide semiconductors. *RSC Adv.* **9**, 25439-25461 (2019).

14 Rivera, P. *et al.* Observation of long-lived interlayer excitons in monolayer $MoSe_2$–WSe_2 heterostructures. *Nat. Comm.* **6**, 6242 (2015).

15 Wang, L. *et al.* One-dimensional electrical contact to a two-dimensional material. *Science* **342**, 614-617 (2013).

16 Nair, R. R. *et al.* Fine structure constant defines visual transparency of graphene. *Science* **320**, 1308-1308 (2008).

17 Chen, X. *et al.* Widely tunable black phosphorus mid-infrared photodetector. *Nature Comm.* **8**, 1672 (2017).

18 Guo, Q. *et al.* Black phosphorus mid-infrared photodetectors with high gain. *Nano Lett.* **16**, 4648-4655 (2016).

19 Liu, Y. *et al.* Gate-Tunable Giant Stark Effect in Few-Layer Black Phosphorus. *Nano Lett.* **17**, 1970-1977 (2017).

20 Long, M. *et al.* Room temperature high-detectivity mid-infrared photodetectors based on black arsenic phosphorus. *Sci. Adv.* **3** (2017).

21 Long, M., Wang, P., Fang, H. & Hu, W. Progress, Challenges, and Opportunities for 2D Material Based Photodetectors. *Adv. Funct. Mater.*, 1803807 (2018).

22 Yu, X. *et al.* Atomically thin noble metal dichalcogenide: a broadband mid-infrared semiconductor. *Nat. Comm.* **9**, 1545 (2018).

23 Qin, D. *et al.* Monolayer $PdSe_2$: A promising two-dimensional thermoelectric material. *Sci. Rep.* **8**, 2764 (2018).

24 Haastrup, S. *et al.* The computational 2D materials database: high-throughput modeling and discovery of atomically thin crystals. 2D Mater. **5**, 042002 (2018).

25 Latini, S., Winther, K. T., Olsen, T. & Thygesen, K. S. Interlayer excitons and band alignment in MoS_2/hBN/WSe_2 van der Waals heterostructures. *Nano Lett.* **17**, 938-945 (2017).

26 Kunstmann, J. *et al.* Momentum-space indirect interlayer excitons in transition metal dichalcogenide van der Waals heterostructures. *Nat. Phys*. **14**, 801-805 (2018).

27 Merkl, P. *et al.* Ultrafast transition between exciton phases in van der Waals heterostructures. *Nat. Mater.* **18**, 691-696 (2019).

28 Fogler, M., Butov, L. & Novoselov, K. High-temperature superfluidity with indirect excitons in van der Waals heterostructures. *Nat. Comm.* **5**, 4555 (2014).

29 Gong, C. *et al.* Band alignment of two-dimensional transition metal dichalcogenides: Application in tunnel field effect transistors. *Appl. Phys. Lett.* **103**, 053513 (2013).

30 Frisenda, R. *et al.* Micro-reflectance and transmittance spectroscopy: a versatile and powerful tool to characterize 2D materials. *J. Phys. D: Appl. Phys.* **50**, 074002 (2017).

31 Rigosi, A. F., Hill, H. M., Li, Y., Chernikov, A. & Heinz, T. F. Probing interlayer interactions in transition metal dichalcogenide heterostructures by optical spectroscopy: MoS_2/WS_2 and $MoSe_2$/WSe_2. *Nano Lett.* **15**, 5033-5038 (2015).

32 Hong, X. *et al.* Ultrafast charge transfer in atomically thin MoS_2/WS_2 heterostructures. *Nat. Nanotechnol.* **9**, 682 (2014).

33 Kozawa, D. *et al.* Evidence for fast interlayer energy transfer in $MoSe_2$/WS_2 heterostructures. *Nano Lett.* **16**, 4087-4093 (2016).

34 Nagler, P. *et al.* Interlayer exciton dynamics in a dichalcogenide monolayer heterostructure. *2D Mater.* **4**, 025112 (2017).

35 Rivera, P. *et al.* Valley-polarized exciton dynamics in a 2D semiconductor heterostructure. *Science* **351**, 688-691 (2016).

36 Baranowski, M. *et al.* Probing the Interlayer Exciton Physics in a MoS_2/$MoSe_2$/MoS_2 van der Waals Heterostructure. *Nano Lett.* **17**, 6360-6365 (2017).

37 Butov, L. V., Shashkin, A. A., Dolgopolov, V. T., Campman, K. L. & Gossard, A. C. Magneto-optics of the spatially separated electron and hole layers in GaAs/$Al_xGa_{1-x}As$ coupled quantum wells. *Phys. Rev. B* **60**, 8753-8758 (1999).

38 Zhang, C., Johnson, A., Hsu, C.-L., Li, L.-J. & Shih, C.-K. Direct Imaging of Band Profile in Single Layer MoS_2 on Graphite: Quasiparticle Energy Gap, Metallic Edge States, and Edge Band Bending. *Nano Lett.* **14**, 2443-2447 (2014).

39 Liu, X. *et al.* Rotationally Commensurate Growth of MoS_2 on Epitaxial Graphene. *ACS Nano* **10**, 1067-1075 (2016).

40 Liu, H. *et al.* Molecular-beam epitaxy of monolayer and bilayer WSe_2: a scanning tunneling microscopy/spectroscopy study and deduction of exciton binding energy. *2D Mater.* **2**, 034004 (2015).

41 Rashba, E. & Gurgenishvili, G. To the theory of the edge absorption in semiconductors. *Sov. Phys. Solid State* **4**, 759 (1962).

42 Rashba, E. A Theory of Impurity Absorption of Light in Molecular Crystals. *Opt. Spektrosk.* **2**, 568-577 (1957).

43 Lau, K. W., Calvin, Gong, Z., Yu, H. & Yao, W. Interface excitons at lateral heterojunctions in monolayer semiconductors. *Phys. Rev. B* **98**, 115427 (2018).

44 Meckbach, L., Huttner, U., Bannow, L., Stroucken, T. & Koch, S. Interlayer excitons in transition-metal dichalcogenide heterostructures with type-II band alignment. *J. Phys.: Condens. Matter* **30**, 374002 (2018).
45 Ross, J. S. *et al.* Interlayer exciton optoelectronics in a 2D heterostructure p–n junction. *Nano Lett.* **17**, 638-643 (2017).
46 Alexeev, E. M. *et al.* Resonantly hybridized excitons in moiré superlattices in van der Waals heterostructures. *Nature* **567**, 81-86 (2019).
47 Ruiz-Tijerina, D. A. & Fal'ko, V. I. Interlayer hybridization and moiré superlattice minibands for electrons and excitons in heterobilayers of transition-metal dichalcogenides. *Phys. Rev. B* **99**, 125424 (2019).
48 Saleh, B. E., Teich, M. C. & Saleh, B. E. *Fundamentals of Photonics*. Vol. 22 (Wiley New York, 1991).
49 Kanazawa, T. *et al.* Few-layer HfS_2 transistors. *Sci. Rep.* **6**, 22277 (2016).
50 Jin, Z., Li, X., Mullen, J. T. & Kim, K. W. Intrinsic transport properties of electrons and holes in monolayer transition-metal dichalcogenides. *Phys. Rev. B* **90**, 045422 (2014).

Acknowledgment. The work is supported by the Agency for Science, Technology and Research (A*STAR) under 2D Materials Pharos Program (Grant No. 152 700014 and Grant No. 152 700017). Q.J.W. acknowledges the funding from the National Research Foundation Competitive Research Program (NRF-CRP18-2017-02 and NRF–CRP19–2017–01). K.S.T. acknowledges support from the Center for Nanostructured Graphene (CNG) under the Danish National Research Foundation (project DNRF103) and from the European Research Council (ERC) under the European Union's Horizon 2020 research and innovation program (Grant No. 773122, LIMA). J.T. and S.L. thank Dr. Chee Wei Lee, Dr. Andrew Ngo and Dr. Meng Zhao for their valuable inputs and Dr. Kedar Hippalgaonkar for sharing tools in device fabrication.

Author contributions. S.L. and J.T. conceived the idea and designed the experiments: S.L., L.D., Q.S.W., and Y.T. performed the experiments: S.L., L.D., Q.J.W and J.T. analysed the data: L.X., A.C.R., G.Z., M.Y., S.L, C.H., L.Y., G.L., H.L., Y.Z., K. S. T., Y.F. contributed to theoretical calculation, S.L., J.T, and Q.J.W. co-wrote the paper. All authors discussed the results and commented on the manuscripts.

Competing interests. The authors declare no competing financial interests.

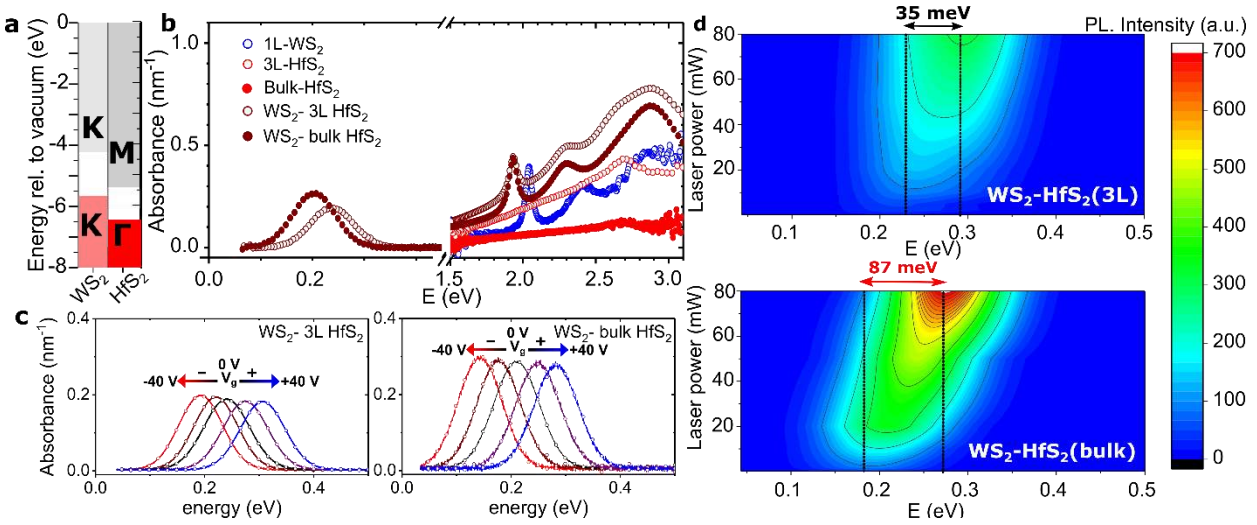

Figure 1. Optical characteristics of interlayer excitons (ILEs) in WS_2-HfS_2 heterostructures. (a) Energy band diagram illustrating valence band maximum (VBM) and conduction band minimum (CBM) of monolayer WS_2 and HfS_2. (b) Absorption spectra of parent material (WS_2 and HfS_2) in the visible range, and the stacked heterostructures in IR and visible range normalised to the thickness. (c) The effect of externally applied voltage (V_g) ranging from -40V to +40V on the absorption spectra of monolayer WS_2 with 3 layers (3L) of HfS_2 and ~30 layers (bulk) HfS_2. (d) The evolution of ILE PL spectra observed in monolayer WS_2 with 3 layers (3L) and ~30 layers (bulk) of HfS_2 as a function of laser power. ILE PL spectra blue-shift with increasing power (excitation density). The shifts are more prominent in bulk HfS_2 than 3L-HfS_2. The ILE energy in WS_2-bulk HfS_2 is lower than WS_2-3L. The PL spectra are bi-Gaussian for 3L-HfS_2 and mono-Gaussian for bulk HfS_2.

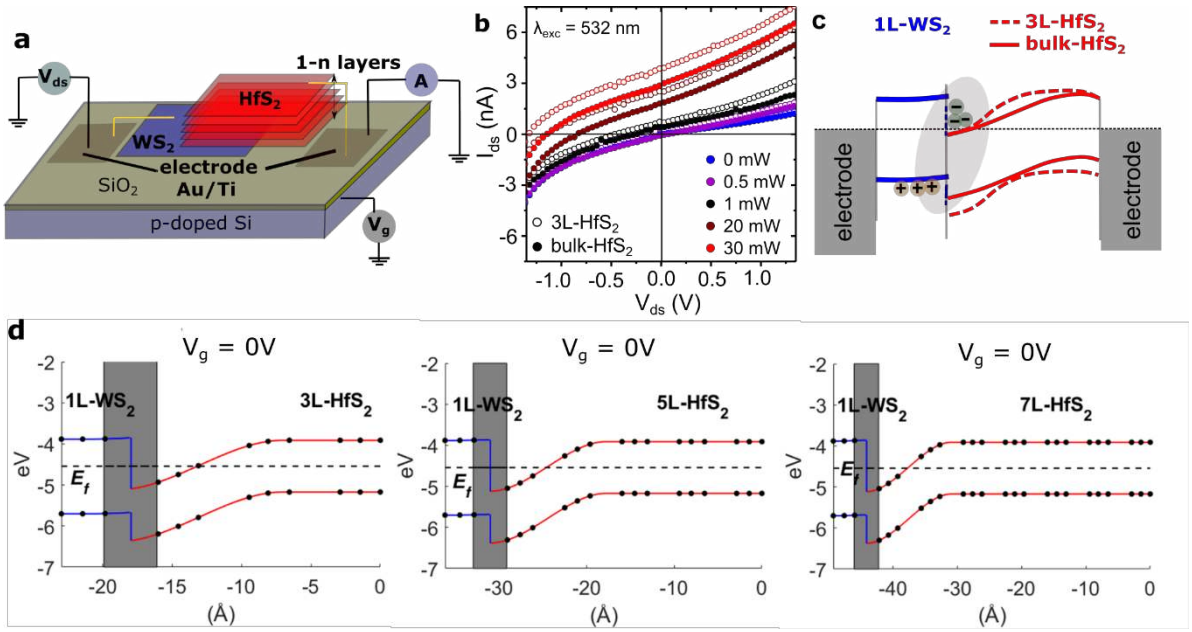

Figure 2. Electrical characterisation of WS_2-HfS_2 interlayer excitons (ILEs) (a) Schematic diagram of the device structure used in this study that consists of exfoliated WS_2 flake with a different number of layers of HfS_2 on a doped silicon substrate, gate voltage (V_g) is applied to control the band alignment and interlayer bandgap. Similarly, drain voltage (V_{ds}) is used for charge extraction when the device is used as photodetectors. (b) *I-V* curve of heterostructure in WS_2-3L and bulk HfS_2 at different excitation power, the curve shifts to the second quadrant with increasing power indicating charge carrier accumulation at the interface. (c) Schematic diagram illustrating the band bending at the interface. Detail of band bending can be found in the main text. We assumed only the VBM of HfS_2 shifts relative to the VBM of WS_2 as the number of layers increases, since the calculation shows the shift in CBM is relatively small. All of the measurements were conducted at room temperature and photo-excitation was achieved by laser with photon energy centered at 2.33 eV. (d) Band profiles of 3L-, 5L- and 7L-HfS_2/1L-WS_2 heterojunction without external bias. The energy reference is set to be the vacuum level (E_{vac} = 0 eV). The highlighted grey-area is the space between the WS_2 and HfS_2. The Fermi level E_F is plotted in black dash line. The black dots denote the location of atoms in out-of-plane direction. WS_2 is slightly n-doped, with the Fermi energy level 0.15 eV above the intrinsic Fermi level (E_{gap} = 1.82 eV).

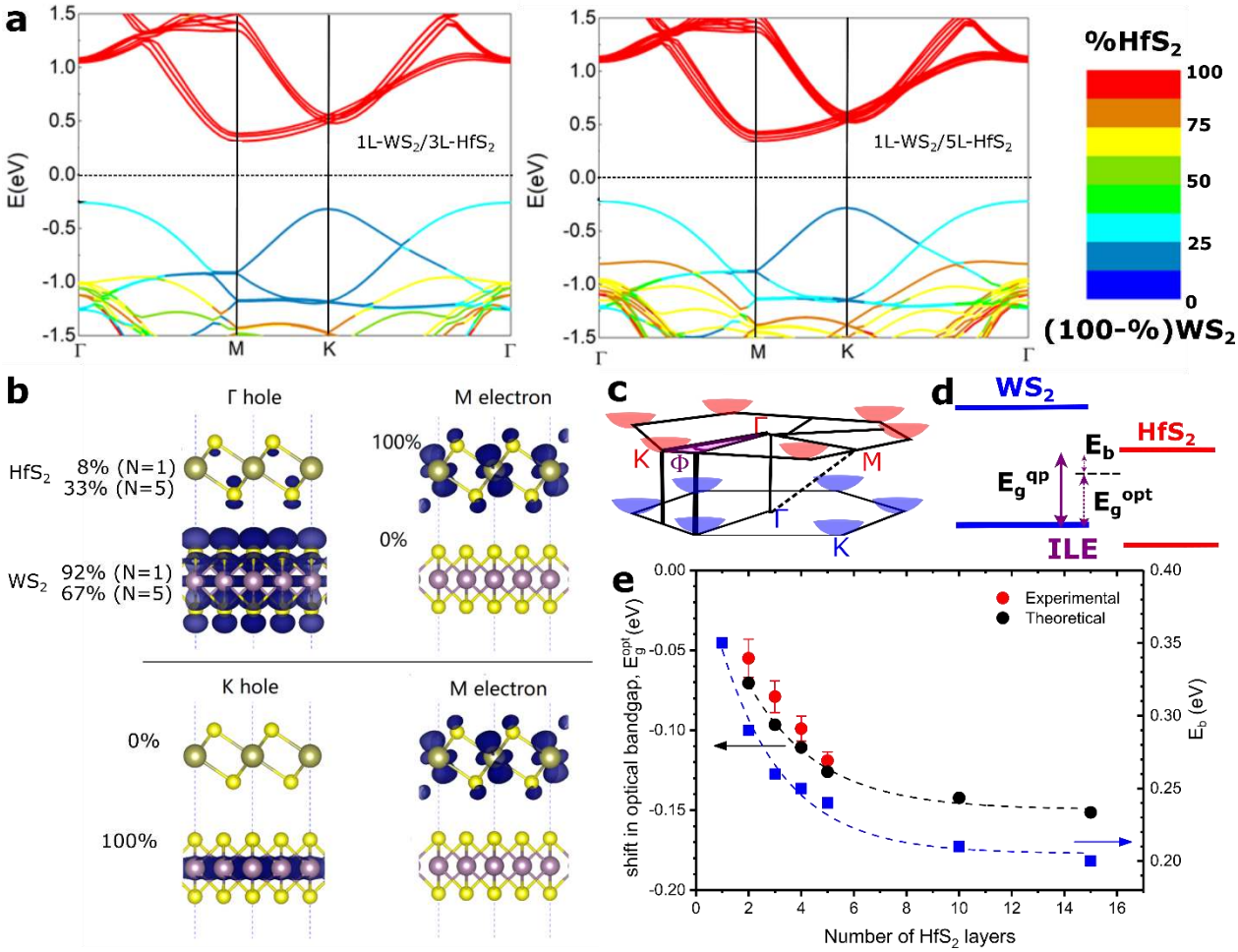

Figure 3. The nature of indirect ILE with large amplitude optical transition. (a) Band structure of WS_2/NLHfS_2 heterostructures for N= 3 and 5 layers of HfS_2 respectively. The color scale denotes the relative contribution of each material to the band states (VBM and CBM) of ILE. (b) The hole and electron states of ILE for Γ-M and K-M transition. While the electron state is localised only in the HfS_2 layer, the hybrid Γ hole state is delocalised over both layers, and the degree of delocalisation increases with the number of HfS_2 layers. Whereas, hole and electron states of K-M transition are localised in the individual layers. (c) The schematic illustration showing the momentum indirect Γ–M transition of the ILE, and the angle stacking mismatch (Φ) between the two 2D materials. (d) Energy diagram showing the correlation between ILE binding energy to the electronic quasi-particle bandgap and optical bandgap, derived from the WS_2 and HfS_2 valence and conduction bands. The large difference in the ILE and intralayer energy prohibits hybridisation and thus explains the angular-independence between the two materials (detail in the text). (e) *Ab-initio* calculated interface exciton binding energy (E_b) as a function of number of HfS_2 layers (blue squares) on the right axis. Black dots and red dots are the theoretical vs. experimental red-shift of the ILE optical band gap (E_g^{opt}) plotted as a function of number of HfS_2 layers. Dashed lines are fitted exponential functions. The mean and the standard deviation of the experimental values are the results of averaging from multiple measurements.

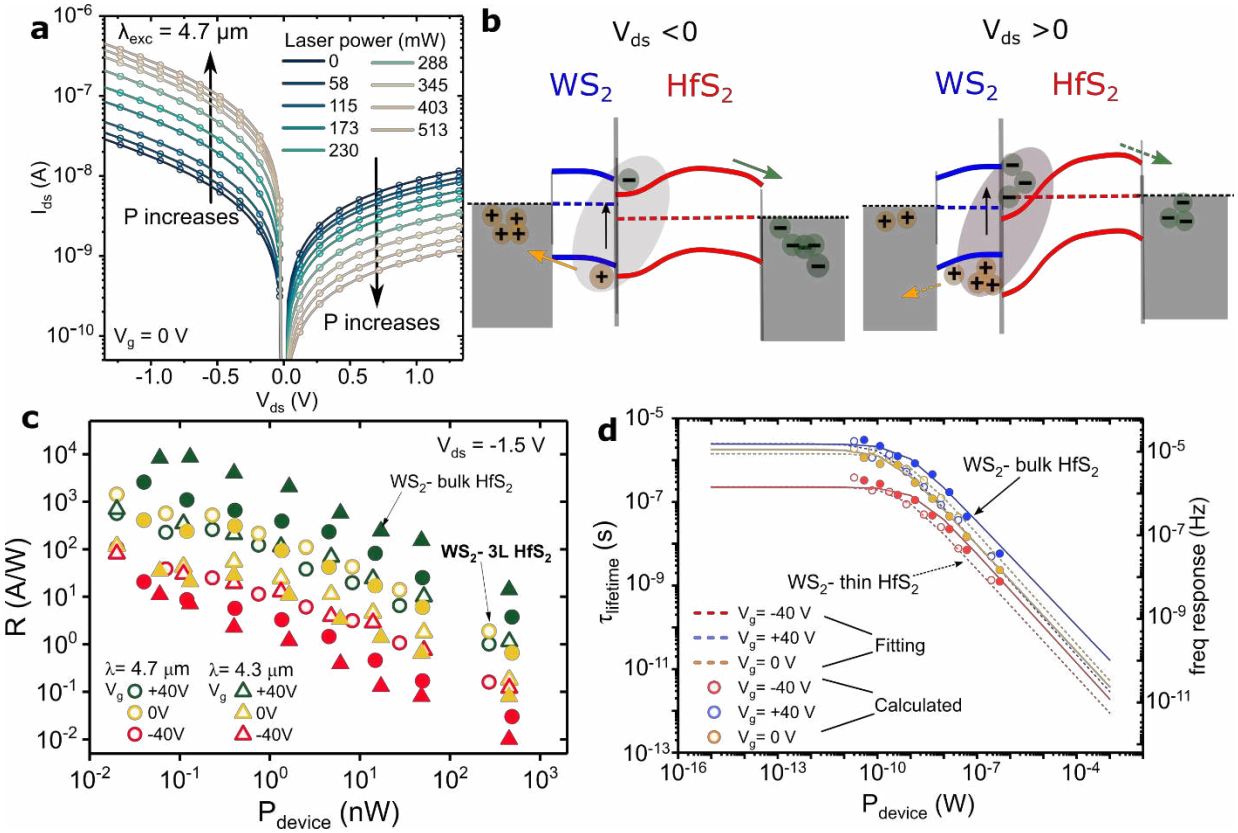

Figure 4. IR Photodetectors based on interface exciton. (a) IV curve of heterostructure in one of the devices made of WS_2 and 3L-HfS_2 under different laser excitation power (λ= 4.7 μm). (b) Schematic diagram illustrating band alignment of WS_2 and HfS_2 under positive and negative source-drain bias (V_{ds}) and the charge extraction process. Under positive V_{ds}, the charge carrier needs to overcome higher energy barrier to move to the electrode. The shade of the ellipses at the interface indicates the strength of recombination. (c) The calculated responsivity (R) of WS_2-3L HfS_2 and WS_2-bulk HfS_2 (one of the devices) under two different excitation wavelengths (λ= 4.3 μm and 4.7 μm) and different gating voltage and V_{ds}=-1.5V. R is defined as I_{ph}/P_{device}. P_{device} is defined as the incident power on the active device, $P_{device} = P_{in}$ *x (L x W/ laser spot size)*, where P_{in} is laser output power, L *x* W are the length and width of the photoactive area rounded to the nearest number. (d) The calculated lifetime of the charge carriers in the device which corresponds directly to the device response time or frequency (Hz), one of the parameters defining the performance of a photodetector. Dashed lines and solid lines are fitting to the data from WS_2-3L HfS_2 and WS_2-bulk HfS_2 devices, respectively. Only the data from device-1 of WS_2-3L HfS_2 and WS_2-bulk HfS_2 are plotted. The data for the remaining devices and detail of calculations can be found in the Supplementary Information.

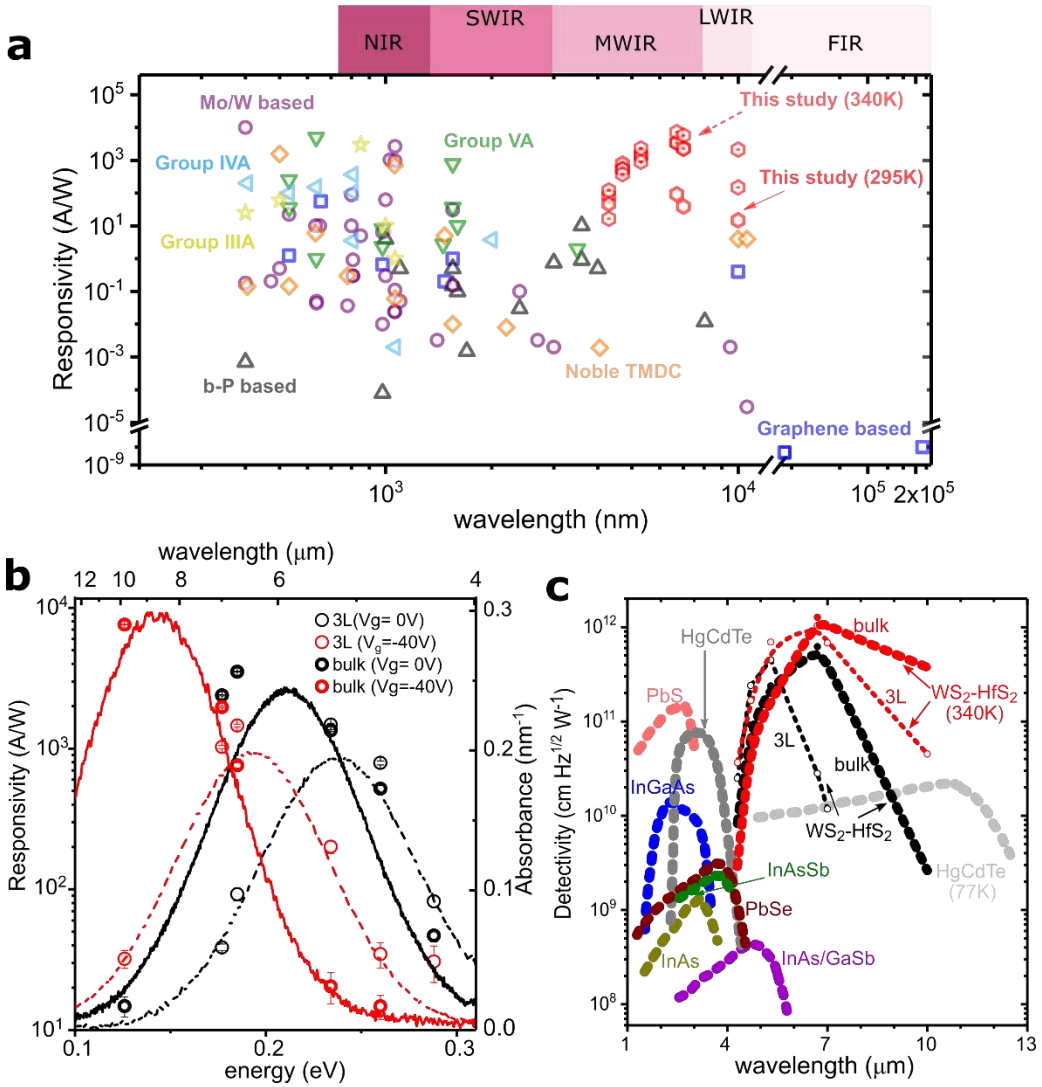

Figure 5. Responsivity and detectivity of IR photodetectors. (a) Comparison of peak responsivity of WS_2-HfS_2 (V_g = 0 V, V_{ds} = -1.5V and P_{device} = 0.5 nW) to other recently reported top-performing 2D-based photodetectors in visible and IR range. References to the selected studies can be found in the Supplementary Information. The fixed large bandgap of most 2D materials limits their application to visible/NIR region. Whereas, the large dark current and small absorption limiting graphene application. (b) The responsivity of WS_2-HfS_2 (V_{ds} = -1.5V and P_{device} = 0.5 nW) at V_g = 0 and -40 V. By tuning the interlayer band alignment and the bandgap, responsivity of the device changes following the shift of ILE absorption peak. The standard deviation is calculated from multiple devices of particular heterostructures. (c) Specific detectivity as a function of wavelength for WS_2-HfS_2 (measured) and the commercially available photodetectors at room temperature, unless otherwise specified. At higher temperatures, the exciton spectral broadening increases the spectral detectivity range, whereas the increase in photon-absorption via phonon-assisted transition increases the detectivity.

Methods

Sample fabrication. Multilayer samples were fabricated by means of a mechanical exfoliation transfer process. For this, we initially exfoliated WS_2 and HfS_2 flakes from bulk crystals (bought from 2Dsemiconductors.com) onto polydimethylsiloxane substrates. Monolayer regions of these flakes were identified via optical microscopy, atomic force microscopy and Raman spectroscopy. Then, we first transferred the WS_2 flake onto the target substrate, a silicon wafer covered with a SiO_2 layer and pre-defined metal markers. Subsequently, the HfS_2 flake was transferred on top of the WS_2. After the transfer, the samples were annealed under Ar gas at 150°C for a few hours.

Optical spectroscopy. The absorption spectra were obtained by reflectance measurements of the samples at room temperature. The reflectance measurements were performed using broadband emission from a tungsten halogen lamp. The spot size on sample was about 2-3 μm. The reflected light was collected by the same objective and deflected by a beam splitter to a spectrometer equipped with a CCD camera cooled to liquid-nitrogen temperature. For λ >1700 nm, we utilised FTIR set-up (Bruker FTIR spectroscopy, Vertex 80v) with HgCdTe detector and Hyperion 2000 microscope to measure the sample reflectance. Commercial Au mirror is used as reference. The reflectance spectra of the samples were determined by normalising them to the reflection spectra of the substrate, which is highly transparent in the wavelength range of interest. Quartz and silicon substrate was used for measurement in visible to near-IR, and mid- to far-IR, respectively. Here, $\Delta R/R = (R_f - R_s)/R_s$, where R_f denotes the reflectance from the sample on substrate, and R_s is the reflectance of the substrate. For thin film, the differential reflectance spectra $\Delta R/R$ is related to the absorption coefficient of the material $\alpha(\lambda)$ as[51,52]:

$$\frac{\Delta R}{R} = \frac{4n}{n_0^2 - 1}\alpha(\lambda) \qquad (1)$$

Where n is the refractive index of the flakes under investigation and n_0 is the refractive index of the substrate. For the heterointerface, the average value of n is used to calculate the absorption coefficient. The values reported in this study are the absorption coefficient of the material normalised to their thickness for impartial comparison.

The PL of the heterostructures in the IR range was measured in the same set-up by exciting the samples with 532 nm laser. Raman and PL (<900nm) measurements were performed in a photon scanning tunneling microscope set-up (Alpha 300S, WITec Gmbh). A CW laser at 532 nm was

coupled to a x50 microscope objective and focused on a submicron spot on the sample surface. PL and scattered light were collected with the same objective, passed through long-pass filters, coupled into a grating spectrometer and detected with a Peltier-cooled CCD. Information was extracted from the spectra by using a fitting routine undertaken manually, which yields the integrated intensity, spectral position and full-width at half maximum for each spectral feature extracted using a Gaussian fit. All of the experiments were performed under low excitation density in order to get a reasonable signal-to-noise ratio and to minimise the generation of trion.

Device structure and characterisation. The metal contact patterns were written using electron beam lithography (Elionx ELS7000) and electron beam evaporator (Denton Vacuum Explorer). The devices were initially coated with polymethyl methacrylate (PMMA) by spin coating at 5000 rpm for 90 s. The post bake was performed at 180°C for 2 min. The design of the electrodes was done with AutoCAD software. The patterns (designed with AutoCAD) were then written with 100 pA current and registration dose of 960μC/cm^2 (0.06μs/dot). The written patterns were developed by using methyl isobutyl ketone (MIBK) and IPA with a developing time of 70 s. The electrode pads consisted of Ti and Au, where Ti was used to improve the adhesion, with thickness of 5 nm and 50 nm, and a deposition rate of 0.1A/s and 1A/s, respectively. The samples were then soaked with acetone for 24 hours for metal contact lift-off. The heterostructures were exfoliated on SiO_2, which provides insulation from the heavily doped silicon backgate. Electrostatic doping is performed by grounding the gold contact and applying a voltage to the backgate (V_g). Furthermore, the silicon chip is glued on a ceramic chip carrier using conductive silver paste. The metal contacts of source and drain as well as the backgate were wire-bonded to the selected pins using metal wires. In a typical measurement, source and back gate are biased by two independent Keithley (2450 and 2420) sourcemeters and drain is the common ground. The sourcemeters are controlled by a computer to measure the current-voltage relation of the device. The responsivity measurement in the IR range is measured with mid-infrared lasers (Tunable CW/Pulsed External Cavity Quantum Cascade Laser). The lasers are focused by IR lens to a final spot size of approximately 100 microns.

Experimental data analysis. For each 2D layer and heterostructure, the absorption and photoluminescence were measured at room temperature, unless specified. To take into account the spatial inhomogeneity of the ILE absorption/emission, spatial averaging was employed. For this, the average absorption/emission energy of the ILE, and its standard deviation, were calculated from the

values extracted from a normal curve fitting routine procedure applied to the spectra collected from the heterostructure regions. On average, 5-10 spectra were evaluated for each individual hetero-structures. Multiple devices were made by stacking the 2D materials together, without any control on the alignment.

Computational methods. The first-principle calculations for the band structure as a function of the number of HfS_2 layers are performed by using Vienna *ab initio* simulation package (VASP)[53] with generalised gradient approximation (GGA) of Perdew-Burke-Ernzerhof (PBE) functional[54] without spin-orbit corrections included. The ion-electron interaction is treated by the PAW method[55], and the van der Waals interaction is taken into consideration using the DFT-D3 method[56]. Electron wave function is expanded on a plane-wave basis set with a cut-off energy of 450 eV. A $6 \times 6 \times 1$ Γ-centered Monkhorst-Pack grid is adopted for Brillouin-zone integration. A vacuum slab of more than 15 Å is applied along the z-direction (normal to the interface) to avoid spurious interaction between repeated slabs. To construct the quasiparticle bandgap at the GW level, a GW calculation is done using GPAW[57,58] for the WS_2 and HfS_2 monolayers with a plane-wave cut-off energy of 800 eV for the ground state and 300 eV for the GW calculation on a 18x18x1 k-point grid including spin-orbit corrections. The quasiparticle band gap is then constructed by correcting the GW monolayer band structures with the N-dependent screening correction calculated from the Quantum Electrostatic Heterostructures (QEH) model[59] and N-dependent hybridisation correction from the PBE band structure calculations for each k-point in each band. This method has previously been shown accurate for calculating band structure of multi-layer van der Waals heterostructures[60]. The interlayer exciton binding energies are calculated by solving the Mott-Wannier equation with the screened electron-hole interaction calculated within the QEH model. The effective electron and hole masses are calculated from the PBE band structures. Structural relaxation is carried out using the conjugate-gradient algorithm until the total energy converges to 10^{-4} eV and the Hellmann-Feynman force on each atom is less than 0.01 eV/Å, respectively.

The calculation of the band diagram of HfS_2 -WS_2 was conducted through the self-consistent calculation for charge density and electric potential in real space. The tight-binding Hamiltonian of 1L-WS_2/3L-HfS_2 was interpolated by the Wannier basis via Wannier90 package[61], where the input was provided from the first-principles results. In the tight-binding Hamiltonian, we considered W-

d, Hf-d and S-p orbitals for the Wannier bases and the Hamiltonian can reproduce bands around the highest valance band and the lowest conduction band obtained from the first-principles calculations. The spatial electric potential was obtained from solving self-consistently the Poisson equation, where the charge density was obtained from the wavefunction of the Wannier tight-binding Hamiltonian. In the self-consistent calculation, we applied the real-space finite element method[62] for numerically solving the Poisson equation, and the relative permittivity (ϵ_r) for HfS_2 and WS_2 are 2[63] and 4.13[64], respectively. In order to approximate the experimental bulk-HfS_2 device, 3L-HfS_2 Hamiltonian was further extended to various numbers of layer of HfS_2. The extension was achieved by inserting n layers of HfS_2 Hamiltonian with interlayer coupling extracting from 3L-HfS_2 layers. 1L-WS_2 was lightly n-doped with the doping concentration ~$1\times10^6 cm^{-2}$ and the HfS_2 was intrinsic. The band profiles were plotted according to the band-edge shifting information given by the calculated electric potential profile

Data availability. The data within this paper are available in public data repository with the following DOI: 10.6084/m9.figshare.12220454[65].

References:

51. Dhakal, K. P. *et al.* Confocal absorption spectral imaging of MoS_2: optical transitions depending on the atomic thickness of intrinsic and chemically doped MoS_2. *Nanoscale* **6**, 13028-13035 (2014).
52. McIntyre, J. & Aspnes, D. E. Differential reflection spectroscopy of very thin surface films. *Surf. Sci.* **24**, 417-434 (1971).
53. Kresse, G. & Furthmüller, J. Efficient iterative schemes for ab initio total-energy calculations using a plane-wave basis set. *Phys. Rev. B* **54**, 11169-11186 (1996).
54. Perdew, J. P., Burke, K. & Ernzerhof, M. Generalized Gradient Approximation Made Simple. *Phys. Rev. Lett.* **77**, 3865-3868 (1996).
55. Blöchl, P. E. Projector augmented-wave method. *Phys. Rev. B* **50**, 17953-17979 (1994).
56. Grimme, S., Antony, J., Ehrlich, S. & Krieg, H. A consistent and accurate ab initio parametrization of density functional dispersion correction (DFT-D) for the 94 elements H-Pu. *J. Chem. Phys.* **132**, 154104 (2010).
57. Mortensen, J. J., Hansen, L. B. & Jacobsen, K. W. Real-space grid implementation of the projector augmented wave method. *Phys. Rev. B* **71**, 035109 (2005).
58. Enkovaara, J. e. *et al.* Electronic structure calculations with GPAW: a real-space implementation of the projector augmented-wave method. *J. Phys: Cond. Matter* **22**, 253202 (2010).
59. Andersen, K., Latini, S. & Thygesen, K. S. Dielectric Genome of van der Waals Heterostructures. *Nano Lett.* **15**, 4616-4621 (2015).
60. Winther, K. T. & Thygesen, K. S. Band structure engineering in van der Waals heterostructures via dielectric screening: the GΔW method. *2D Mater.* **4**, 025059 (2017).
61. A. A. Mostofi, J. R. Yates, G. Pizzi, Y. S. Lee, I. Souza, D. Vanderbilt, and N. Marzari, *Comp. Phys. Comm.* **185,** 2309 (2014).
62. COMSOL, Inc., LiveLink™ for MATLAB User's Guide LiveLink™ for MATLAB® User's Guide.
63. Chen, Q. Y., Liu, M. Y., Cao, C., & He, Y. Engineering the electronic structure and optical properties of monolayer 1T-HfX2 using strain and electric field: A first principles study. *Physica E Low Dimens. Syst. Nanostruct.* **112**, 49-58 (2019).
64. Ghosh, Ram Krishna, and Santanu Mahapatra. "Monolayer transition metal dichalcogenide channel-based tunnel transistor." *IEEE J. Electron Devi.* **1**(10), 175-180 (2013).
65. Lukman, S. & Teng, J.. High Oscillator Strength Interlayer Excitons in 2D Heterostructures for Mid-IR Photodetection. https://doi.org/10.6084/m9.figshare.12220454.v1 (2020).

Additional Information. Supplementary information is available in the online version of the paper. Reprints and permission information is available online at www.nature.com/reprints. Correspondence and requests for materials should be addressed to J.T.